Society of Medical Education & Research

2025, Volume 5, Issue 1, Page No: 1-17
ISSN: 3108-4834

Archive of International Journal of Cancer and Allied Science

Small-Molecule Inhibition of SOST Suppresses Breast Cancer Bone Metastasis

Yousef Hamdan Khalil[1]*, Omar Salman Nassar[1]

[1]Department of Oncology, University of Jordan Hospital, Amman, Jordan.

***E-mail** ✉ y.khalil.ujh@outlook.com

Abstract

Osteoporosis can worsen breast cancer metastasis to bone, correlates with poor long-term prognosis, and currently has limited treatment options. Sclerostin (SOST), a natural inhibitor of bone formation, represents a promising target for osteoporosis therapy. Nevertheless, it remains uncertain whether SOST could serve as a therapeutic target for breast cancer bone metastases, and if small-molecule agents that modulate SOST in breast cancer cells can suppress bone metastasis. SOST levels were assessed in 442 breast cancer specimens via immunohistochemistry, and statistical analyses were conducted to evaluate the correlation with bone metastasis. Bone-metastatic SCP2 breast cancer cells were subjected to SOST knockdown or overexpression, and their metastatic behaviors in bone were examined both in vitro and in vivo. To explore potential therapeutic strategies, we screened small-molecule inhibitors targeting the SOST-STAT3 interaction and evaluated the anti-tumor and anti-metastatic effects of one lead compound in vitro and in vivo. Elevated SOST expression correlated with breast cancer bone metastasis and poorer patient survival. Knockdown of SOST notably decreased the bone metastatic potential of SCP2 cells. Mechanistically, SOST bound STAT3 to activate TGF-β/KRAS signaling, promoting tumor proliferation and bone metastasis. Administration of the candidate compound, S6, markedly suppressed the growth of breast cancer organoids and bone metastases in murine models. These results identify a novel therapeutic avenue for addressing bone metastasis in breast cancer.

Keywords: Bone metastasis, Small-molecule compound, SOST, Breast cancer

Introduction

Every year, over 1.5 million individuals worldwide are affected by cancer metastasis to bone [1]. These patients often endure severe skeletal complications, including fractures, debilitating pain, and functional limitations, which markedly impair quality of life [2]. Evidence indicates that osteoporosis is a notable risk factor for bone metastasis in cancer [3], and anti-osteoporotic therapies have long been utilized in managing patients with skeletal metastatic disease.

Access this article online https://smerpub.com/

Received: 11 October 2024; **Accepted:** 14 January 2025

How to cite this article: Khalil YH, Nassar OS. Small-Molecule Inhibition of SOST Suppresses Breast Cancer Bone Metastasis. Arch Int J Cancer Allied Sci. 2025;5(1):1-17. https://doi.org/10.51847/XR3tpAzZri

Agents targeting bone, such as bisphosphonates, are known to limit osteolytic activity and enhance the bone microenvironment, thereby suppressing metastatic progression. However, in the phase III SUCCESS trial, bisphosphonates failed to prevent bone metastases in early-stage breast cancer patients [4]. Although some reports indicate that bisphosphonates may slow breast cancer cell proliferation [5, 6], they have not been shown to directly eradicate tumor cells within bone lesions. Several osteosecretory proteins play central roles in osteoporosis, prompting the development of therapeutic antibodies to inhibit both bone resorption and metastasis. Denosumab, an antibody targeting RANKL, can postpone the occurrence of SREs and slow disease progression in patients with metastatic bone disease [7], but it does not directly kill tumor cells at metastatic sites. Sclerostin (SOST), a glycoprotein secreted by mature osteocytes in the bone matrix [8], functions as a potent

inhibitor of bone formation and represents a promising therapeutic target for osteoporosis [9-12]. Beyond its role in bone metabolism, SOST has been implicated as an oncogenic factor, driving breast cancer bone metastasis and osteolysis; inhibiting SOST has been shown to mitigate tumor-induced bone damage and associated muscle weakness [13, 14]. Romosozumab, a humanized antibody against SOST, is FDA-approved for osteoporosis [15] and works by binding SOST in the stromal compartment to stimulate osteogenesis [16]. While highly effective for postmenopausal osteoporosis, clinical trials have noted elevated cardiovascular risks [17, 18]. Therefore, there is a pressing need to discover novel SOST inhibitors, particularly small-molecule compounds, that are safe and effective for treating both osteoporosis and cancer bone metastases.

In this study, we demonstrate that elevated SOST expression correlates with poorer outcomes in breast cancer patients. Mechanistically, SOST promotes tumor cell proliferation and metastasis to bone through activation of downstream signaling pathways. Using computational approaches, we identified a small-molecule compound capable of disrupting the SOST-STAT3 interaction, inhibiting STAT3 activation, and reducing breast cancer bone metastasis.

Materials and Methods

Patient cohort

A total of 422 breast cancer patients, along with 69 matched pairs of primary tumors and corresponding metastatic lesions, were enrolled at Shengjing Hospital of China Medical University between April 2011 and July 2013. Diagnoses were confirmed through radiological imaging and pathological evaluation. Patients were excluded if clinical data were incomplete, if they had received neoadjuvant therapy, had another malignancy, severe organ dysfunction, or bilateral breast cancer. Tumor tissues obtained during surgery were fixed in 10% formalin, embedded in paraffin, and prepared for histology and immunohistochemistry (IHC). Written informed consent was obtained, and the study protocol was approved by the Institutional Research Ethics Committee (Project ID 2018PS304K, approved 03/05/2018).

Histological analysis

Tissue sections (4 μm) were deparaffinized, rehydrated, and stained with hematoxylin and eosin (H&E). Slides were visualized using a light microscope (Olympus, Tokyo, Japan) and independently assessed by two blinded pathologists.

Immunohistochemistry

Sections (4 μm) were deparaffinized, rehydrated, and treated with 3% H2O2 in methanol. Antigen retrieval was performed in citrate buffer (pH 6.0) using a microwave for 10 minutes. After blocking with 5% bovine serum albumin (BSA) in TBST, sections were incubated with mouse anti-SOST antibody (ab63097, Abcam, Cambridge, MA, USA) at 25 °C for 2 hours. Bound antibodies were detected with HRP-conjugated goat anti-mouse IgG for 30 minutes, visualized using 3,3′-diaminobenzidine, and counterstained with hematoxylin. Staining intensity and frequency were quantified using IHC Profiler software [19].

Cell culture

Human breast cancer cell lines MDA-MB-231 and MCF-7, along with mouse osteogenic precursor MC3T3-E1 cells, were obtained from ATCC (Manassas, VA, USA). SCP2 cells were kindly provided by Professor Joan Massague (Howard Hughes Medical Institute, Memorial Sloan-Kettering Cancer Center, NY, USA). MDA-MB-231 cells were maintained in Leibovitz's L15 medium (Thermo Fisher, Carlsbad, CA, USA), MCF-7 cells in DMEM with 10% FBS (Biological Industries, Cromwell, CT, USA), and MC3T3-E1 cells in α-MEM supplemented with 10% FBS and 1% P/S. All cells were cultured at 37 °C with 5% CO2 in a humidified incubator.

Transduction

SCP2 cells (1 × 10^7 per well) were exposed to lentiviral particles at a multiplicity of infection (MOI) of 10 to introduce either a control shRNA or an SOST-targeting shRNA carrying green fluorescent protein (GFP) (Sangon Biotech, Shanghai, China). Cells were cultured in the presence of 5 μg/mL puromycin (A1113803, Thermo Fisher) for seven days to generate stable SCP2/NC and SCP2/KD cell lines. The efficiency of SOST knockdown was verified by Western blotting. The shRNA sequences used were: SOST KD1, 5'-GCAGTGAAAGATGTAGCCAAA-3'; SOST KD2, 5'-GCCTCAGATAATCTGGTGAAA-3'. The SOST coding sequence was obtained from GenBank, and primers were designed as follows: SOST-F (EcoRI): AGGGAGACCCAAGCTGGCTAGTTGaattcGCCACC ATGCAGCTCCCACT; SOST-R (BamHI):

GTCACTTAAGCTTGGTACCGAggatccGTAGGCGT TCTCCAGCTCGGC. Subsequently, the SOST cDNA fragment was cloned into a pcDNA3.1-CMV-MCS-3flag-EF1-ZsGreen-T2A-Puro vector and sequence-verified. MDA-MB-231 cells were transfected with either the empty vector or the SOST-expressing construct, followed by G418 selection, producing stable SOST-overexpressing MDA-MB-231/OE cells and control MDA-MB-231/NC cells. Protein expression levels were determined using Western blot analysis.

Quantitative real-time RT-PCR (qRT-PCR)

Total RNA was extracted from SCP2/KD, SCP2/NC, MDA-MB-231/OE, and MDA-MB-231/NC cells using TRIzol (Thermo Fisher) and converted into cDNA. Gene expression levels were normalized to GAPDH and quantified with TB Green Premix Ex Taq II (RR820A, Takara) using a PrimeScript RT Master Mix (RR047A, Takara) according to the manufacturer's instructions. Relative gene expression was calculated using the 2^−ΔΔCt method.

Western blotting

Whole-cell lysates from MDA-MB-231, SCP2, MCF-10A, SCP2/NC, and SCP2/KD cells were prepared in RIPA buffer and centrifuged at 1000 × g for 20 minutes at 4 °C. Protein concentrations were measured using a bicinchoninic acid assay kit (Thermo Fisher). Lysates (40 µg per lane) were resolved by 12% SDS-PAGE and transferred onto PVDF membranes (MilliporeSigma, Burlington, MA, USA). Membranes were blocked with 5% BSA in TBST and incubated overnight at 4 °C with primary antibodies against SOST (ABIN6997488, antibodies-online GmbH, Germany), TGF-β (ER31210, HuanBio, Hangzhou, China), SMAD3 (66516–1-1 g, PTG, Rosemont, USA), CXCR4 (60042–1-1 g, PTG), STAT3 (10253–2-AP, PTG), phospho-STAT3 (9138, Cell Signaling Technology), KRAS (12063–1-AP, PTG), and β-actin (20536–1-AP, PTG). HRP-conjugated secondary antibodies (1:10,000; Jackson ImmunoResearch, West Grove, PA, USA) were used for detection. Signal visualization was performed using enhanced chemiluminescence (Thermo Fisher), and relative protein levels were quantified using ImageJ software (NIH, Bethesda, MD, USA).

Immunoprecipitation (IP)

SCP2 cells were lysed in ice-cold RIPA buffer containing protease inhibitors, and cell debris was removed by centrifugation. Lysates (50 µg per tube) were incubated overnight at 4 °C with 2 µg of anti-SOST, anti-STAT3, or control IgG antibodies. For S6 treatment, lysates (1 mL) were preincubated with 200 µM S6 for 1 hour at room temperature prior to antibody incubation. Immunocomplexes were captured using 20 µL of protein A/G plus-agarose beads (sc-2003, Santa Cruz, USA) at 4 °C for 4 hours, washed with TBST, and eluted in 2× SDS loading buffer. Samples were subjected to SDS-PAGE and analyzed with anti-SOST or anti-STAT3 antibodies to confirm protein-protein interactions.

Enzyme-linked immunosorbent assay (ELISA)

SCP2 cells were co-cultured with MC3T3-E1 cells (5 × 10^5 per well) in 6-well plates and treated with either DMSO or S6 for 24 hours. Supernatant CXCL12 levels were measured using an ELISA kit (KE10049, PTG) with 3,3',5,5'-tetramethylbenzidine, following the manufacturer's protocol. Experiments were performed in triplicate. Absorbance at 450 nm was measured using a microplate reader (Biotek, USA), and CXCL12 concentrations were determined from a standard curve generated with recombinant CXCL12.

Chemotaxis assay

To assess migratory behavior, 3 × 10^4 breast cancer cells were suspended in 200 µL of medium supplemented with 2% FBS and placed in the upper compartment of a 24-well transwell insert (3422, Corning, USA). MC3T3-E1 cells, cultured to ~80% confluence in 200 µL of 2% FBS medium, occupied the lower compartment. After 24 hours of co-culture, non-migrated cells on the upper membrane were removed with a cotton swab. Cells that traversed the membrane to the lower surface were fixed with 0.5% crystal violet (v/v) and quantified by observers blinded to treatment conditions.

Adhesion assay

To create a bone-like microenvironment, MC3T3-E1 cells were osteogenically differentiated in α-MEM containing 10% FBS, 10 mM β-glycerophosphate (Solarbio), and 50 µg/mL ascorbic acid (Solarbio) for nine days. The resulting matrix was treated with 20 mM NH4OH (Sigma, USA) and 0.5% Triton X-100 (Solarbio) for five minutes to generate a mineralized surface. GFP-labeled breast cancer cells (2 × 10^5 per well) were seeded onto the prepared matrix and allowed to adhere for 15 minutes. Non-adherent cells were

removed by aspiration, and attached cells were washed with PBS and counted using fluorescence microscopy.

Cell viability and cytotoxicity assay

Proliferation and cytotoxicity of SCP2/WT, SCP2/NC, SCP2/KD1, SCP2/KD2, MDA-MB-231, and MCF-7 cells were assessed using the Cell Counting Kit-8 (CCK8, Dojindo, Japan). Cells were plated in 96-well plates and incubated for 24, 48, or 72 hours with or without S6 at different concentrations, or with positive controls of 50 μM epirubicin (EADM) or 5 nM docetaxel (DTX). During the final four hours of incubation, a 10% CCK8 solution was added. Absorbance at 450 nm was measured with a microplate reader (Biotek, USA).

Biolayer interferometry (BLI)

Binding between S6 and SOST was measured using an Octet K2 instrument (ForteBio) at 30 ºC with continuous shaking at 1000 RPM in a buffer containing 0.1% BSA, 0.01% Tween-20, and 1% DMSO in PBS, as described previously [20]. Recombinant SOST (10593-H07H, SinoBio, Beijing, China) at 0.15 mg/mL was biotinylated and immobilized onto SSA biosensors. S6 (C29H24N6O2S, MW 520.62, Chemdiv, USA) was prepared in PBS at different concentrations. Each association/dissociation cycle was followed by a 10-minute wash with buffer to remove nonspecific binding. Kinetic constants (kon, koff) and the equilibrium dissociation constant (Kd) were calculated using the instrument's software with double reference subtraction.

Murine xenograft tumor model

Female BALB/c nude mice were used to generate a model of breast cancer bone metastasis [21]. Each mouse received 1 × 10^6 SCP2/WT, SCP2/NC, or SCP2/KD cells via intracardiac injection (n = 8–10 per group). Body weights were recorded over 42 days, and tumor colonization in bone was monitored weekly using X-ray and bioluminescence imaging. Survival was assessed daily.

For therapeutic evaluation, mice bearing SCP2 cells were randomized to receive intravenous injections of vehicle (5% DMSO in PBS) or S6 at 10 mg/kg twice weekly for 42 days. Body weights were measured every other day. Mice were euthanized if they lost 20–25% of body weight or developed cachexia or severe wasting. Tumors from bones and vertebrae were dissected, imaged with microCT, fixed, decalcified, embedded, and sectioned for H&E staining. Osteoclast activity was assessed by TRAP staining (387A, Sigma). Heart, liver, spleen, lung, bone marrow, and kidney tissues were collected for H&E staining to evaluate potential S6 toxicity. All procedures were conducted following the NIH Guide for the Care and Use of Laboratory Animals and approved by the Institutional Research Ethics Committee of Shengjing Hospital of China Medical University (Project ID 2020PS318K, approved 04/01/2020).

Molecular modeling and docking

The full-length structure of STAT3 (residues A135–L731) was reconstructed using crystallographic data (PDB: 6QHD) together with the Alphafold2 model (UniProt: P40763) via Modeller 9.22, generating 1,000 candidate models. Quality assessment employed DOPE, Molpdf, DFIRE2, and Procheck scores, followed by a 50-ns molecular dynamics (MD) relaxation to stabilize the structure.

From the SOST NMR structure (PDB: 2K8P), two loop regions corresponding to β-sheets (residues 75–81 and 132–138) were selected for docking with the relaxed STAT3 structure. Protein–protein docking was performed using Zdock, emphasizing specific residues to guide interaction predictions. The highest-scoring complex was refined through a 100-ns MD simulation to optimize its conformation.

MD simulations were carried out with Gromacs 2020.4 using the Amber14 force field. The protein complex was placed in a cubic TIP3P water box with 1-nm padding and neutralized by adding sodium and chloride ions. Energy minimization was conducted in two steps. The system was gradually heated to 300 K over 100 ps, equilibrated under NVT for 2 ns and NPT for 5 ns. Production MD was performed at 300 K and 1 atm with the LINCS algorithm constraining hydrogen bond lengths, allowing a 2-fs timestep. Trajectory coordinates and energies were saved every 10 ps. MM-PBSA binding energy calculations were conducted using gmx_MMPBSA [22].

Virtual screening

The equilibrated SOST structure from MD simulations served as the basis for identifying potential ligand-binding pockets using FTSite [23] and FTMap [24]. Screening was performed using FIPSDock [25] against a chemical library. The geometric center of SOST defined the grid, covering 200 × 200 × 160 points at 0.375 Å spacing. Only the lowest-energy docked poses for each binding mode were selected. Among the top 200 candidates, S6 was highlighted. The SOST–S6 complex

underwent a 500-ns MD simulation to verify stability and binding mode.

Organoid drug sensitivity assay

Breast tumor specimens were obtained from a patient at Shengjing Hospital of China Medical University with informed consent. Tissues were minced and digested in 50-mL tubes containing 20 mL AdDF+++ medium (Advanced DMEM/F12, 1× Glutamax, 10 mM HEPES, 1% P/S) and 2 mg/mL collagenase at 37 °C for 2 hours with agitation. Following centrifugation at 400 g for 10 min, the tissue was mechanically dissociated with pipetting (10, 5, 1 mL tips) and resuspended in 10 mL AdDF+++ with 2% FBS to form organoids. Cell suspensions were mixed with Matrigel (1:2 ratio) and 100 µL was plated per well in 24-well plates, solidifying at 37 °C for 30 min under 5% CO2. Medium was replaced every 3 days, and organoids were passaged weekly. Only organoids maintained for >3 passages and showing robust growth were used. Organoids were treated with 2 µM or 80 µM S6 or left untreated (NS) for 48 hours. Morphology and cytotoxicity were examined using an inverted microscope (Nikon, Japan).

BMSC differentiation

Mouse BMSCs (2 × 10^5 per well) were plated in 12-well plates and induced toward osteogenic differentiation using α-MEM supplemented with 10% FBS, 50 µg/mL L-ascorbic acid, 1 mM dexamethasone, and 1 M β-glycerophosphate, in the presence of DMSO or 8 µM S6. Media were refreshed every 2 days for 14 days. Cells were fixed with 4% paraformaldehyde, permeabilized with 0.1% Triton X-100, and stained for ALP (Sigma-Aldrich). Some cultures were extended to 21 days and stained with alizarin red. Mineralized nodules were solubilized with 10% cetylpyridinium chloride for 2 hours under gentle shaking. Relative absorbance of S6-treated samples versus DMSO control (set to 1) was calculated.

Transcriptome sequencing and promoter analysis

Total RNA from SCP2/NC and SCP2/KD1 cells was extracted and sequenced on the Illumina platform (Biomarker Technologies, Beijing, China). Gene expression was quantified using FPKM and DESeq2. Differentially expressed genes (DEGs) were defined as $|\log2FC| > 1$ with FDR < 0.05. KEGG pathway annotation was used to analyze functional implications. STAT3 binding motifs within the TGF-β and KRAS promoter regions were predicted using rVista 2.0 and the JASPAR database [26].

Statistical analysis

Results are expressed as mean ± SEM. One-way ANOVA with Newman-Keuls post hoc test was used for multi-group comparisons, while Student's t-test was applied for pairwise comparisons. Kaplan–Meier analysis and log-rank tests evaluated DMFS. Cox regression was employed for univariate and multivariate survival analysis. Analyses were conducted with SPSS 23.0 (IBM, Armonk, NY, USA), with significance defined as $P < 0.05$.

Results and Discussion

Elevated SOST expression correlates with breast cancer bone metastasis

Characterizing phenotypic markers of breast cancer bone metastasis is crucial for improving clinical management. To explore this, SOST protein levels were examined in 422 primary breast cancer specimens via immunohistochemistry (IHC). High SOST expression was observed in 24.2% (102/422) of the samples and was significantly linked to poorer overall survival (OS) and disease-free survival (DFS) ($P < 0.001$), **(Figure 1a).** Similar trends were found across different molecular subtypes of breast cancer and within the triple-negative breast cancer (TNBC) cohort from TCGA.

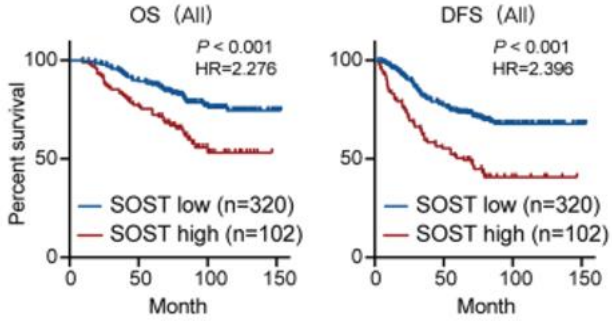

a)

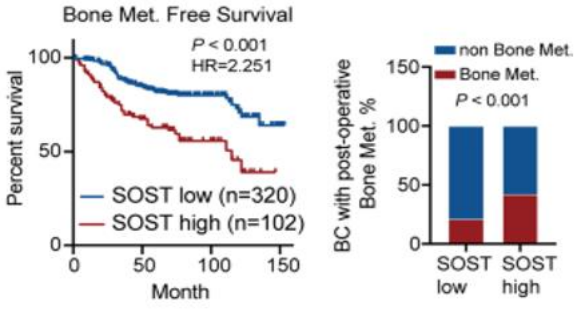

b)

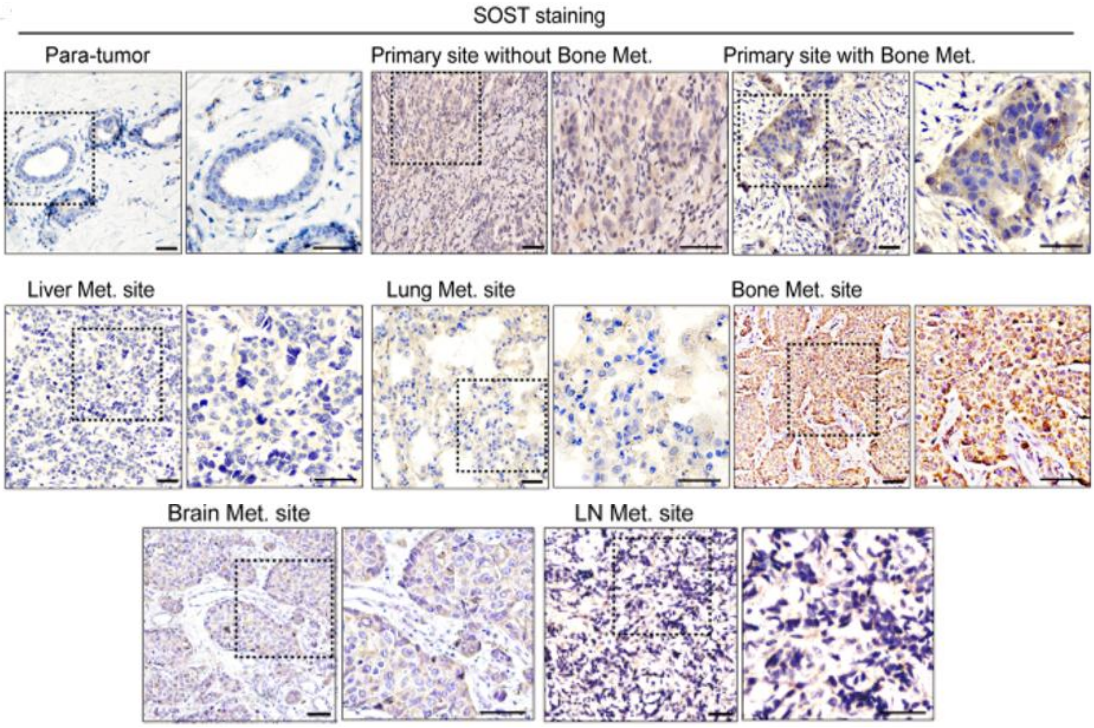

c)

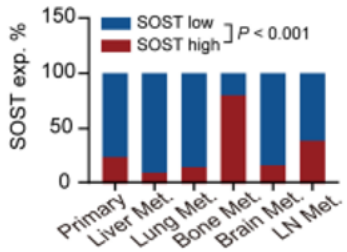

d)

Figure 1. Upregulation of SOST correlates with bone metastasis and poorer prognosis in breast cancer patients. a) Overall survival (OS) and disease-free survival (DFS) for patients with high versus low SOST expression in breast tumors ($P < 0.001$), analyzed using a two-sided log-rank test. b) Bone metastasis-free survival (BMFS) and the incidence of bone metastases in patients stratified by SOST expression ($P < 0.001$), determined by a two-sided log-rank test. c) Representative immunohistochemistry (IHC) images of SOST in normal breast tissue, primary breast tumors (n = 422), liver metastases (n = 10), lung metastases (n = 20), bone metastases (n = 15), brain metastases (n = 15), and lymph node metastases (n = 15); scale bar, 100 μm. d) Quantitative analysis of SOST levels corresponding to the samples shown in panel c.

Further investigation revealed that patients with tumors expressing high SOST levels experienced shorter bone metastasis-free survival (BMFS) and were more prone to developing bone metastases compared with patients whose tumors had lower SOST expression **(Figure 1b).** IHC evaluation of 69 paired primary tumors and metastatic lesions across multiple organs demonstrated that SOST expression was elevated in both primary tumors and bone metastases relative to normal breast tissue or tumors without bone involvement. In contrast, SOST levels were lower in liver and lung metastases **(Figures 1c and 1d),** reinforcing its role in bone-specific metastasis. Additionally, SOST expression showed a positive correlation with N stage and postoperative distant metastases, particularly to bone ($P < 0.01$), but not to lung, liver, or brain **(Table 1)**. No significant

relationships were observed with T stage, ER, PR, HER2 status, Ki67, molecular subtype, or menopausal status **(Table 1).**

Univariate and multivariate Cox regression analyses identified high SOST expression, menopausal status, N stage, and ER/PR positivity—but not T stage, HER2 status, Ki67, or molecular subtype—as independent predictors of worse distant metastasis-free survival (DMFS) ($P < 0.01$), **(Table 2)**. These results suggest that SOST may serve as a specific biomarker for predicting bone metastasis in breast cancer patients.

Table 1. Correlation between SOST expression and clinicopathological characteristics in breast cancer patients

Characteristic	P-value	Total (n = 422)	SOST High Expression (%)	SOST Low Expression (%)
T stage	0.133			
T1		123 (29.15)	35 (28.46)	88 (71.54)
T2		283 (67.06)	61 (21.55)	222 (78.45)
T3		16 (3.79)	6 (37.50)	10 (62.50)
N stage	0.006			
N0-1		328 (77.73)	69 (21.04)	259 (78.96)
N2–3		94 (22.27)	33 (35.11)	61 (64.89)
ER status	0.636			
ER negative		149 (35.31)	38 (25.50)	111 (74.50)
ER positive		273 (64.69)	64 (23.44)	209 (76.56)
PR status	0.734			
PR negative		200 (47.39)	50 (25.00)	150 (75.00)
PR positive		222 (52.61)	52 (23.42)	170 (76.58)
HER2 status	0.165			
HER2 negative		251 (59.48)	67 (26.69)	184 (73.31)
HER2 positive		171 (40.52)	35 (20.47)	136 (79.53)
Ki67 status	0.570			
Ki67 < 20%		193 (45.73)	44 (22.80)	149 (77.20)
Ki67 ≥ 20%		229 (54.27)	58 (25.33)	171 (74.67)
Molecular type	0.395			
HR+ HER2-		188 (44.55)	48 (25.53)	140 (74.47)
HR+ HER2+		95 (22.51)	18 (18.95)	77 (81.05)
HR- HER2+		76 (18.01)	17 (22.37)	59 (77.63)
TNBC		63 (14.93)	19 (30.16)	44 (69.84)
Distant metastasis^a	< 0.001			
No		272 (64.45)	45 (16.54)	227 (83.46)
Yes		150 (35.55)	57 (38.00)	93 (62.00)
Bone metastasis	< 0.001			
No		313 (74.17)	59 (18.85)	254 (81.15)
Yes		109 (25.83)	43 (39.45)	66 (60.55)
Lung metastasis	0.282			
No		374 (88.63)	87 (23.26)	287 (76.74)
Yes		48 (11.37)	15 (31.25)	33 (68.75)
Liver metastasis	0.155			
No		397 (94.08)	93 (23.43)	304 (76.57)
Yes		25 (5.92)	9 (36.00)	16 (64.00)
Brain metastasis	0.686			
No		414 (98.10)	101 (24.40)	313 (75.60)
Yes		8 (1.90)	1 (12.50)	7 (87.50)
Menopause status	0.300			
Premenopausal		172 (40.76)	37 (21.51)	135 (78.49)
Postmenopausal		250 (59.24)	65 (26.00)	185 (74.00)

Data are presented as n (%).

HR: Hormone receptor; ER: Estrogen receptor; PR: Progesterone receptor; HER2: Human epidermal growth factor receptor 2; TNBC: Triple-negative breast cancer.

a Distant metastasis indicates cases with confirmed distant metastasis by the end of the follow-up period.

Table 2. Evaluation of factors associated with distant metastasis-free survival (DMFS)

Variable	Multivariate Analysis		Univariate Analysis	
	Hazard Ratio (95% CI)	P-value	Hazard Ratio (95% CI)	P-value
SOST × menopause status	2.12 (1.46–3.08)	< 0.001	2.59 (1.80–3.73)	< 0.001
T stage		0.917		0.660
T2 vs. T1	1.00 (0.68–1.47)	0.988	1.02 (0.71–1.46)	0.926
T3 vs. T1	1.19 (0.51–2.79)	0.696	1.44 (0.65–3.21)	0.374
N stage	4.15 (2.94–5.88)	< 0.001	4.38 (3.16–6.06)	< 0.001
ER × PR	0.54 (0.35–0.82)	0.004	0.60 (0.43–0.83)	0.002
HER2	0.66 (0.38–1.16)	0.150	0.99 (0.72–1.38)	0.969
Ki67	0.98 (0.69–1.39)	0.895	0.98 (0.71–1.34)	0.877
Molecular type		0.331		0.910
HR+ HER2+ vs. HR+ HER2-	0.68 (0.43–1.08)	0.103	0.90 (0.59–1.38)	0.645
HR- HER2+ vs. HR+ HER2-	0.66 (0.38–1.16)	0.150	1.09 (0.70–1.69)	0.706
TNBC vs. HR+ HER2-	0.82 (0.45–1.48)	0.503	0.96 (0.60–1.56)	0.879

DMFS Distant metastasis-free survival, *HR* Hormone receptor, *CI* Confidence interval, *ER* Estrogen receptor, *PR* Progesterone receptor, *HER2* Human epidermal growth factor receptor 2, *TNBC* Triple-negative breast cancer. × represents joint analysis

SOST knockdown suppresses tumor growth and bone metastasis

Primary tumors and their corresponding metastatic lesions often share key genetic features, suggesting that metastases can originate from dominant clones in the primary tumor [27]. SCP2 breast cancer cells, derived from a single MDA-MB-231 cell through repeated left ventricular injection in mice, exhibit a strong bone-metastatic phenotype [28]. To determine the role of SOST in this bone-specific tropism, protein levels were compared among SCP2, MDA-MB-231, and MCF-7 cells by Western blot. SCP2 cells displayed markedly higher SOST expression than the other two cell lines **(Figure 2a)**. Immunofluorescence staining further revealed that SOST was predominantly localized in the cytoplasm of SCP2 cells **(Figure 2b).**

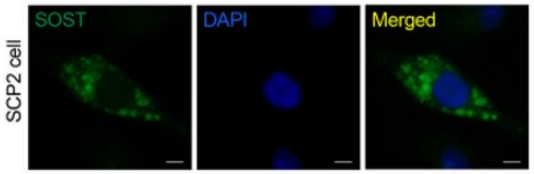

b)

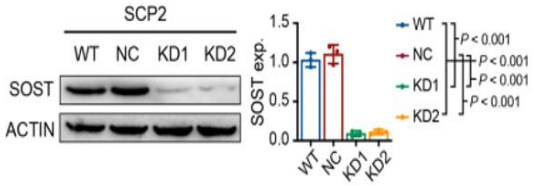

c)

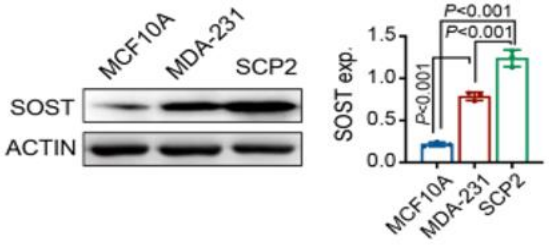

a)

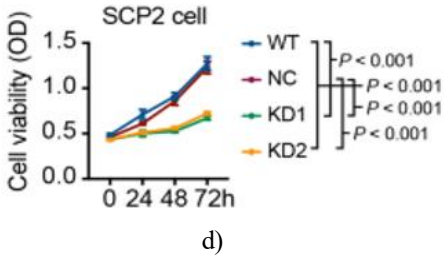

d)

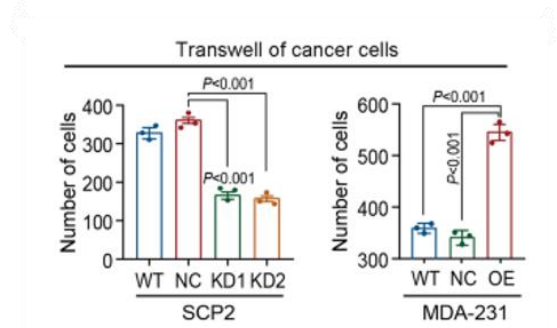

e)

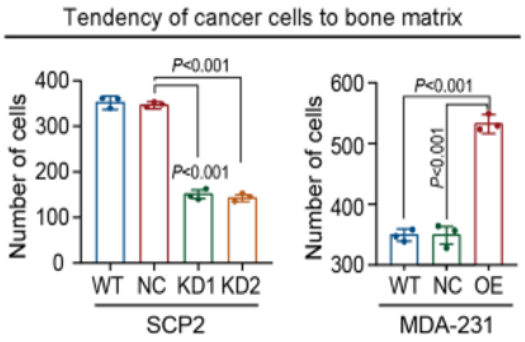

f)

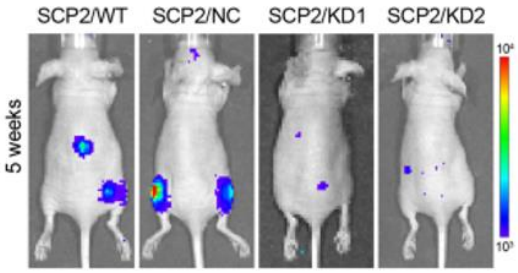

g)

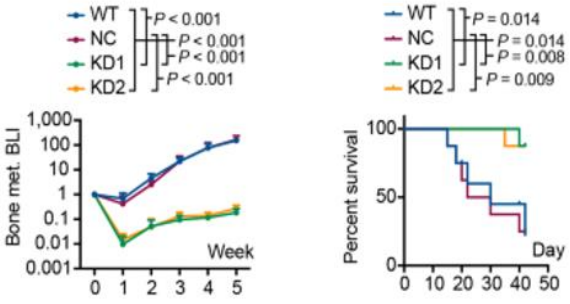

h)

Figure 2. SOST knockdown reduces migration and bone metastasis of breast cancer cells
a–b) Western blotting showed SOST protein levels in MCF10A, MDA-MB-231, and SCP2 cells, and immunofluorescence revealed cytoplasmic localization in SCP2 cells (SOST, green; DAPI, blue). c) Knockdown efficiency of shSOST in SCP2 cells was verified by Western blot. d) CCK-8 assays demonstrated reduced proliferation following SOST silencing. e–f) Migration and adhesion assays revealed decreased movement toward MC3T3-E1 cells and reduced adhesion to bone matrix for SCP2/KD cells, while SOST-overexpressing MDA-MB-231 cells showed enhanced behavior. g–h) Bioluminescence imaging and survival analysis of BALB/c-nu mice following left-ventricular injection of WT, NC, or SCP2/KD cells (n = 8–10 per group).

To evaluate SOST function, SCP2 cells were stably transduced with lentivirus expressing shSOST, reducing SOST levels by ~85% ($P < 0.001$), **(Figure 2c).** Functionally, SOST knockdown significantly inhibited SCP2 proliferation in vitro **(Figure 2d)**, though basal migratory capacity remained unaffected. Compared with unmodified SCP2 and SCP2/NC cells, SCP2/KD cells exhibited markedly reduced chemotaxis toward osteogenic MC3T3-E1 cells, whereas SOST-overexpressing MDA-MB-231 cells displayed enhanced migration **(Figure 2e)**. A similar trend was observed in adhesion assays on the bone matrix **(Figure 2e)**. In vivo, left-ventricular injection of SCP2/KD cells led to substantially fewer osteolytic lesions **(Figure. 2g)** and prolonged mouse survival over 5 weeks compared to SCP2/WT or SCP2/NC injections **(Figure 2h).** These results indicate that SOST is critical for bone matrix adhesion and bone metastasis.

SOST promotes SCP2 cell proliferation and chemotaxis via STAT3, enhancing TGF-β and KRAS signaling

To clarify the mechanisms through which SOST influences SCP2 cell proliferation, RNA sequencing was conducted on SOST/NC and SOST/KD1 cells. Differentially expressed genes (DEGs) in SOST/KD1 cells were analyzed with Cluster3.0 using lgRPKM values **(Figure 3a)**. KEGG pathway enrichment was assessed by gene ratio, FDR, and the number of genes involved **(Figure 3b)**. The data suggested that SOST modulates TGF-β/SMAD3 signaling, and knocking down SOST decreased the mRNA levels of RAS and TGF-β in SCP2 cells **(Figure 3c)**. Considering SOST's cytoplasmic localization and its role in promoting cell proliferation, we propose that SOST may trigger RAS and TGF-β pathways via interactions with intracellular transcription factors such as STAT3. STAT3 binding

sites within KRAS and TGF-β promoter regions were predicted using rVista 2.0 in the JASPAR database [26] **(Figure 3d)**. Furthermore, GEPIA database analysis revealed that STAT3 expression positively correlates with KRAS, NRAS, and MRAS, as well as TGFB2, SMAD2, and SMAD3 in breast cancer samples.

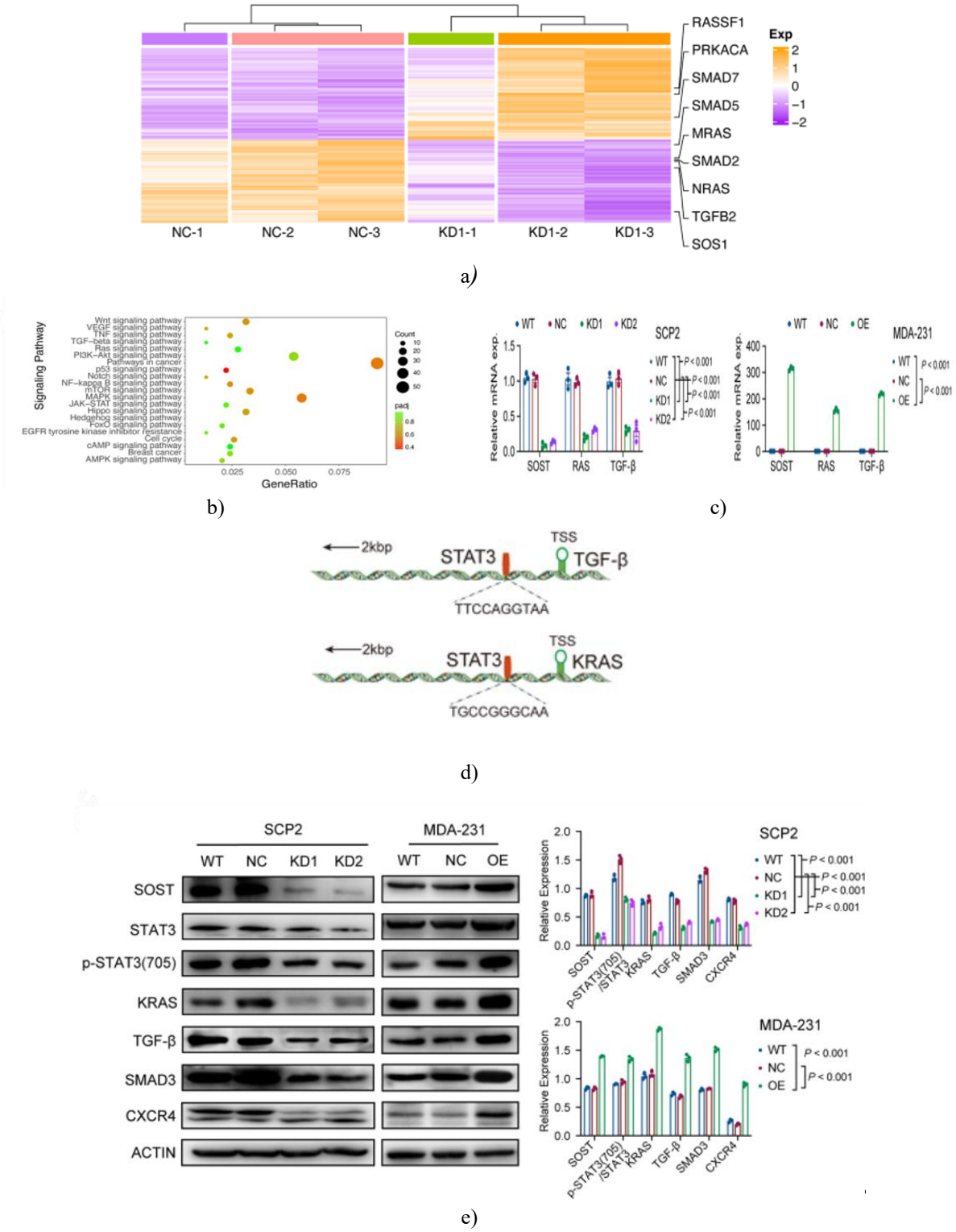

Figure 3. SOST facilitates bone metastasis via TGF-β/SMAD3 signaling.

a) Heatmap illustrating the DEGs between WT and SOST-silenced SCP2 cells following RNA sequencing. b) KEGG pathway analysis of DEGs identified after SOST knockdown in SCP2 cells. c) qRT-PCR quantification of relative mRNA levels of SOST, KRAS, and TGFB in WT versus SOST-silenced SCP2 cells and WT versus SOST-over-expressing MDA-MB-231 cells. d) Diagram showing predicted STAT3 binding sites in the promoters of TGFB and KRAS based on rVista 2.0 software. e) Western blot analysis of SOST, KRAS, TGF-β, SMAD3, CXCR4, and STAT3 relative to β-actin, as well as STAT3 phosphorylation in the indicated SCP2 or MDA-MB-231 cells.

Since TGF-β/SMAD3 signaling is known to enhance CXCR4 expression in breast cancer cells, facilitating metastasis, and considering that its ligand CXCL12 is abundant in the bone marrow microenvironment, we investigated whether silencing SOST affects these pathways in SCP2 cells. SOST knockdown markedly reduced STAT3 phosphorylation at Y705 and lowered the expression of TGF-β, RAS, SMAD3, and CXCR4 **(Figure 3e)**. Conversely, overexpression of SOST in MDA-MB-231 cells with initially low SOST levels produced opposite effects **(Figure 3e)**. Collectively, these findings indicate that SOST may drive SCP2 cell proliferation through activation of TGF-β/RAS signaling and promote bone metastasis by elevating CXCR4 levels.

Identification of small-molecule SOST inhibitors to disrupt stat3 interaction

We modeled SOST–STAT3 interactions to screen potential inhibitors from a small-molecule library **(Figure 4a)**. Modeling predicted that Y705 of STAT3 could dock within a pocket of SOST **(Figure 4b)**. Virtual screening of ~120,000 compounds yielded 38 candidates. Single-concentration BLI assays were conducted for all but three poorly soluble compounds (2, 10, 25) **(Table 1)**. Nine candidates (6, 11, 12, 17, 22, 24, 34, 38) were further evaluated via multi-concentration assays to determine R^2, Kd, k_dis, and response **(Figures 4d and 4e) (Table 2).** Four compounds (6, 11, 28, 34) were advanced for drug sensitivity testing **(Figure 4f)**, with compound 6 (S6) exhibiting potent, dose- and time-dependent inhibition of SCP2 proliferation **(Figure 4f)**. BLI confirmed strong binding of S6 to SOST **(Figure 4g)**. Structural modeling showed S6 occupying the SOST–STAT3 pocket **(Figures 4h–4i),** likely preventing their interaction. Co-immunoprecipitation experiments validated that S6 disrupted SOST–STAT3 binding in SCP2 cells **(Figure 4j)**.

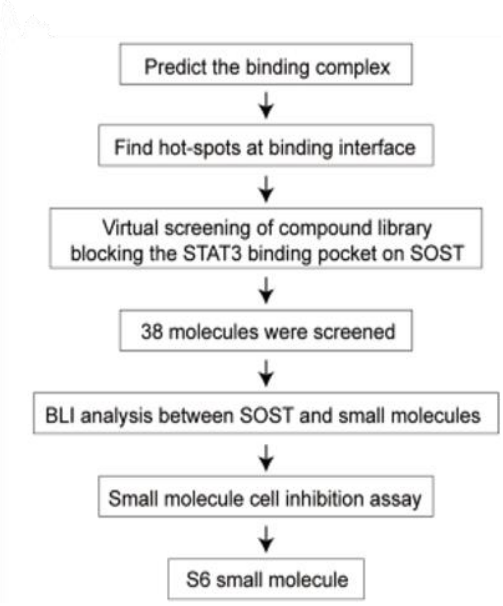

a)

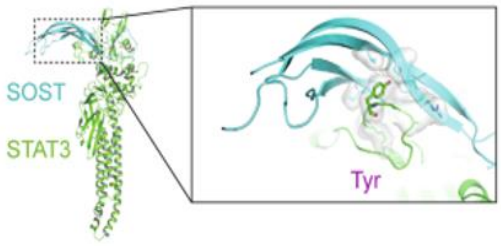

b)

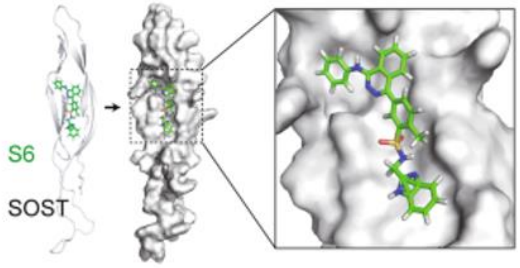

c)

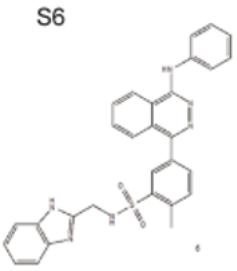

d)

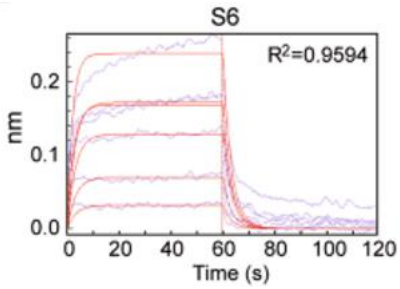

e)

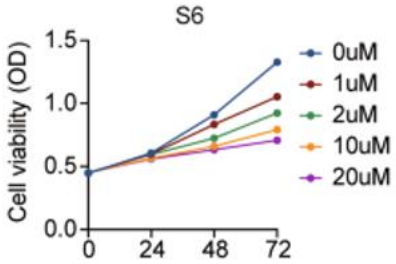

f)

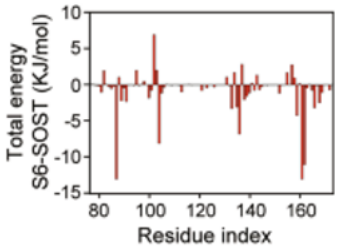

g)

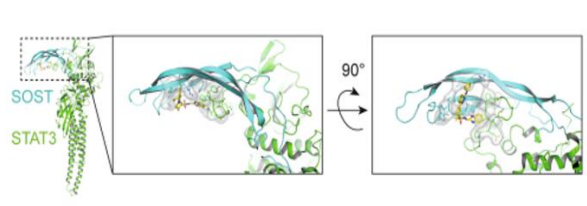

h)

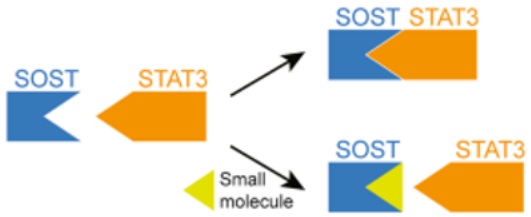

i)

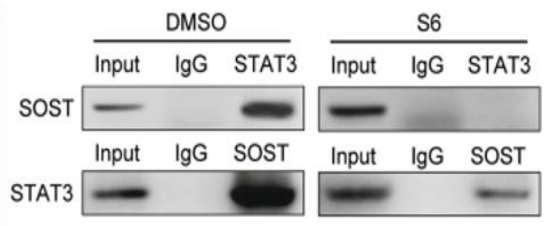

j)

Figure 4. Identification of S6, a small molecule targeting SOST

a) Workflow illustrating computational identification of compounds that obstruct STAT3–SOST binding. b) Depiction of the interaction interface between SOST and STAT3. **c)** Predicted docking of S6 into the SOST binding pocket. **d)** Chemical structure of compound 6, designated S6. **e)** Multi-concentration binding analysis of S6 (K_D = 3.992E-04, R^2 = 0.9594). f) Effect of S6 on SCP2 cell proliferation. g–h) Energy profile and structural model of the SOST–S6–STAT3 complex. i) Conceptual illustration showing S6 blocking the SOST–STAT3 interface. j) Co-immunoprecipitation confirms that S6 disrupts SOST–STAT3 binding in SCP2 cells.

S6 suppresses breast cancer cell growth

The anti-tumor potential of S6 was evaluated in vitro and in vivo. SCP2 cells treated with S6 showed markedly reduced proliferation, with an IC_{50} of 1.89 μM (95% CI: 1.27–2.74) **(Figure 5a).** At 2 μM, S6 exhibited stronger growth inhibition than 50 μM EADM or 5 nM DTX in SCP2 cells **(Figure 5b)**, and similar effects were observed in MCF-7 and MDA-MB-231 cells. In organoid models, 80 μM S6 for 48 h suppressed proliferation effectively, comparable to conventional chemotherapeutics **(Figure 5c)**. In animal experiments, S6 treatment improved survival in tumor-bearing mice **(Figure 5d)** and promoted body weight maintenance **(Figure 5e)**. No obvious structural damage was detected in major organs, indicating minimal toxicity. Mechanistically, S6 reduced STAT3 phosphorylation and downregulated TGF-β, KRAS, SMAD3, and

CXCR4 expression in SCP2 cells **(Figure 5f)**, indicating suppression of the TGF-β/KRAS/STAT3 pathway and inhibition of tumor progression.

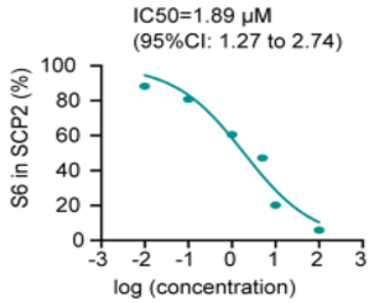

a)

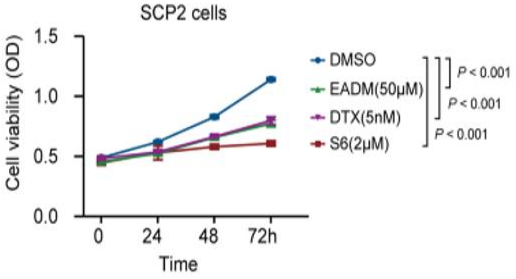

b)

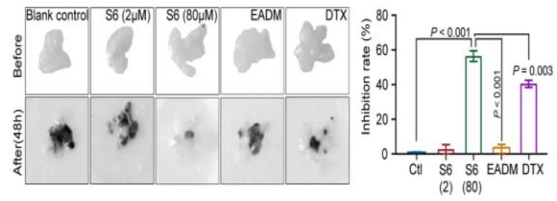

c)

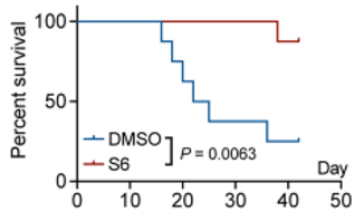

d)

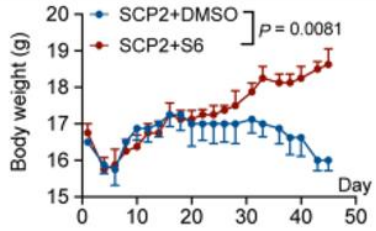

e)

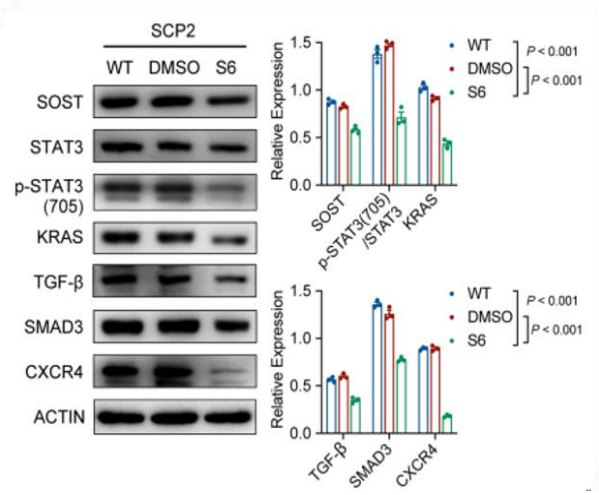

f)

Figure 5. S6 inhibits breast cancer cells and tumor growth

a) IC_{50} of S6 in SCP2 cells (1.89 μM, 95% CI: 1.27–2.74) measured by CCK-8. b) Comparison of cell viability after treatment with 2 μM S6, DMSO, 50 μM EADM, or 5 nM DTX. c) Growth inhibition of organoids treated with 80 μM S6 for 48 h (38.96%, 95% CI: 37.01–40.89) versus 2 μM S6 (0.53%, 95% CI: 0.12–0.92), EADM (500 μM), or DTX (250 nM). d) Survival of SCP2 tumor-bearing mice treated with S6 or DMSO (n = 8–10 per group, P = 0.0063). e) Mouse body weights following 45-day treatment with DMSO or 10 mg/kg S6 (P = 0.0081). f) Western blot showing SOST, KRAS, TGF-β, SMAD3, CXCR4, STAT3 levels and STAT3 phosphorylation after 48 h of treatment.

S6 attenuates breast cancer bone metastasis

The effect of S6 on bone metastasis was further investigated. ALP and ARS staining indicated that S6 enhanced osteoblastic differentiation of BMSCs **(Figures 6a and 6b)**. In vivo, S6 preserved bone integrity in tumor-bearing mice **(Figure 6c)** and reduced osteoclast activity, as shown by H&E and TRAP staining **(Figure 6d)**. Both S6 and the CXCR4 inhibitor AMD3100 decreased SCP2 migration toward MC3T3-E1 cells in vitro **(Figure 6e)**, and S6 lowered CXCL12 concentrations in the co-culture supernatant **(Figure 6f)**. Importantly, S6 treatment reduced the incidence of bone metastasis in SCP2 tumor-bearing mice **(Figure 6g)**. Collectively, these results indicate that S6 occupies the STAT3-binding pocket on SOST, thereby disrupting downstream TGF-β/KRAS/CXCR4 signaling and

inhibiting the proliferation and metastasis of SCP2 cells **(Figure 6h)**.

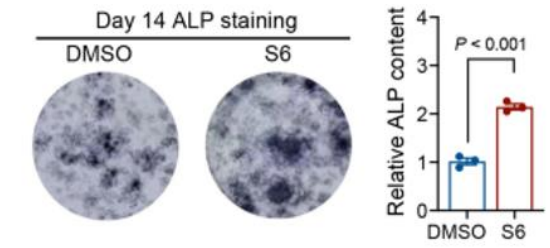

a)

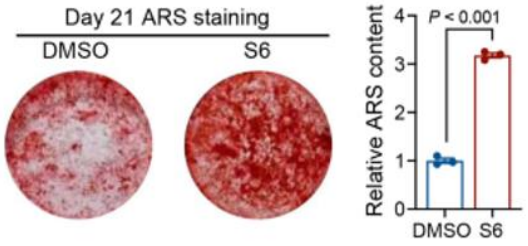

b)

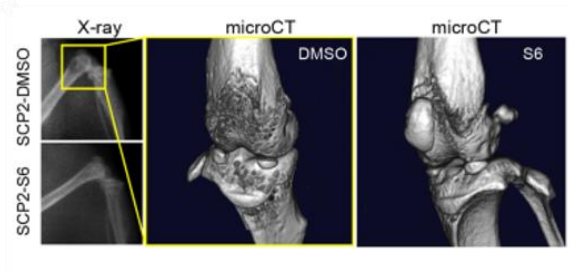

c)

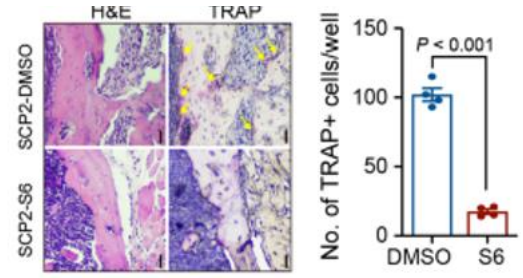

d)

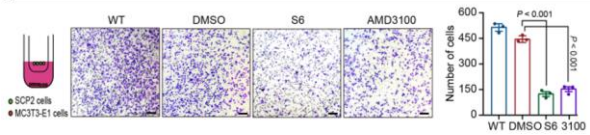

e)

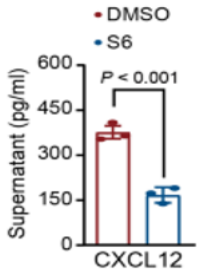

f)

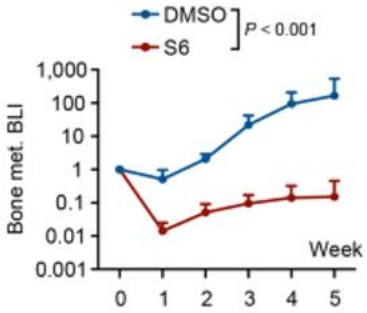

g)

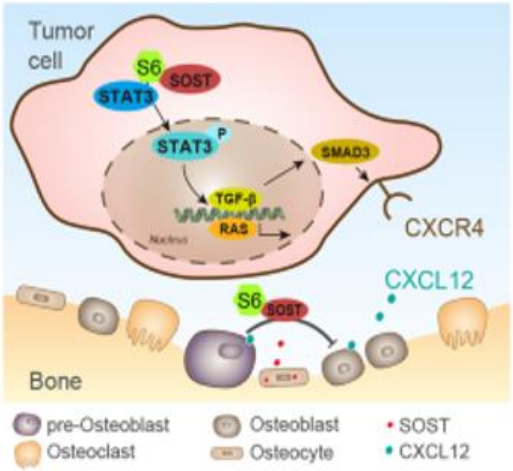

h)

Figure 6. S6 suppresses bone metastasis in breast cancer models

a–b) ALP and ARS staining demonstrating enhanced osteogenic differentiation after 2 μM S6 treatment for 14 and 21 days, respectively. c) Representative X-ray and microCT images showing bone lesions in SCP2 tumor-bearing mice treated with DMSO or 10 mg/kg S6**.** d) H&E and TRAP staining of bone metastases. e) Transwell assays showing that S6 or AMD3100 reduced SCP2 migration toward MC3T3-E1 cells. f) Reduction of CXCL12 levels in supernatants of SCP2/MC3T3-E1 co-cultures following S6 treatment**.** g) Bioluminescent

imaging 5 weeks after intraventricular injection of SCP2 cells, showing decreased metastasis in S6-treated mice (n = 8–10 per group). h) Schematic model illustrating how SOST activates STAT3, RAS, and TGF-β/SMAD/CXCR4 signaling to promote proliferation and osteotropism, whereas S6 blocks this interaction and suppresses metastasis.

Skeletal-related events (SREs) are a leading contributor to morbidity and mortality in cancer patients [29]. Current therapeutic approaches for bone metastases include external radiotherapy, chemotherapy, endocrine treatments, targeted drugs, and radionuclide-based therapies (NCCN 2022 version). While chemotherapy, endocrine therapy, and certain bone-targeted agents (BTAs) have direct anticancer activity, BTAs such as bisphosphonates and denosumab primarily act by inhibiting host cell responses, particularly osteoclasts, to tumor-secreted factors [29]. Osteoclasts are central to therapeutic strategies for skeletal metastases regardless of the tumor origin [30]. Clinically employed BTAs include bisphosphonates, RANKL inhibitors like denosumab, and bone-seeking radionuclides (radium, strontium, samarium), which mainly suppress bone resorption without directly targeting tumor cells.

Characterizing the phenotypic traits of breast cancer bone metastases is crucial for improving therapeutic strategies. Despite advances in understanding the metastatic cascade, there remains a need for additional targeted therapies. Prior studies reported increased circulating SOST levels in breast cancer patients, particularly in triple-negative breast cancer (TNBC) [14, 31]. In our cohort of 422 breast cancer patients, elevated SOST expression in primary tumors was strongly associated with bone metastasis, supporting its role as a pro-metastatic factor [13, 14] and highlighting SOST as a potential therapeutic target for bone dissemination.

From a translational perspective, SOST-neutralizing antibodies were previously shown to suppress the bone metastatic niche and improve survival in tumor-bearing mice [13, 14]. However, these antibodies had a limited impact on primary tumor growth. Using bone-tropic SCP2 breast cancer cells [32], we demonstrated that SOST enhances tumor cell proliferation through activation of the STAT3/TGF-β/KRAS signaling axis. These findings provide proof-of-concept that SOST is a viable target for both primary tumor control and inhibition of bone metastasis.

Importantly, we identified a small-molecule compound capable of disrupting the SOST-STAT3 interaction. Protein–protein interactions (PPIs) play critical roles in biological processes, including cancer initiation and progression [33]. While targeting PPIs was once considered challenging due to their large and flat interfaces [34], structural studies have revealed that only a subset of "hot spot" residues contributes the majority of binding energy, allowing the rational design of PPI inhibitors [35, 36]. Consistently, our structural analyses confirmed that the SOST-STAT3 interface depends on several key residues, making it susceptible to small-molecule inhibition.

Notably, currently approved SOST monoclonal antibodies for osteoporosis predominantly target loop 2 of SOST, which is linked to cardiovascular safety [37]. Targeting loop 2 can increase cardiovascular risks, similar to romosozumab. In contrast, S6 was designed to bind a non-loop 2 pocket of SOST and exhibited excellent tolerability in vivo with minimal toxicity, avoiding cardiotoxicity. Structural modeling and co-immunoprecipitation confirmed that S6 binds SOST and competes with STAT3, effectively disrupting the SOST-STAT3 complex in breast cancer cells. Mechanistically, S6 occupies a critical SOST pocket, preventing STAT3-mediated pro-tumor signaling.

Conclusion

In summary, our results demonstrate that the SOST-STAT3 complex is a druggable target for breast cancer bone metastasis. S6 emerges as a promising candidate for further development, representing a novel class of therapeutics with potential to inhibit both tumor progression and skeletal dissemination.

Acknowledgments: We sincerely respect Prof. Joan Massague for his significant contributions to the field of cancer bone metastasis and thank him for providing SCP2 cells.

Conflict of Interest: None

Financial Support: This work was supported by grants from the National Natural Science Foundation of China (81872159, 81902607), and 345 Talent Project of Shengjing Hospital of China Medical University.

Ethics Statement: None

References

1. Weilbaecher KN, Guise TA, McCauley LK. Cancer to bone: a fatal attraction. Nat Rev Cancer. 2011;11:411–25.
2. Macedo F, Ladeira K, Pinho F, Saraiva N, Bonito N, Pinto L, Goncalves F. Bone Metastases: An Overview. Oncol Rev. 2017;11:321.
3. Drake MT. Osteoporosis and cancer. Curr Osteoporos Rep. 2013;11:163–70.
4. Friedl TWP, Fehm T, Muller V, Lichtenegger W, Blohmer J, Lorenz R, Forstbauer H, Fink V, Bekes I, Huober J, et al. Prognosis of patients with early breast cancer receiving 5 years vs 2 years of adjuvant bisphosphonate treatment: a phase 3 randomized clinical trial. JAMA Oncol. 2021;7:1149–57.
5. Fromigue O, Lagneaux L, Body JJ. Bisphosphonates induce breast cancer cell death in vitro. J Bone Miner Res. 2000;15:2211–21.
6. De Rosa G, Misso G, Salzano G, Caraglia M. Bisphosphonates and cancer: what opportunities from nanotechnology? J Drug Deliv. 2013;2013: 637976.
7. Stopeck AT, Lipton A, Body JJ, Steger GG, Tonkin K, de Boer RH, Lichinitser M, Fujiwara Y, Yardley DA, Viniegra M, et al. Denosumab compared with zoledronic acid for the treatment of bone metastases in patients with advanced breast cancer: a randomized, double-blind study. J Clin Oncol. 2010;28:5132–9.
8. Moester MJC, Papapoulos SE, Löwik CWGM, van Bezooijen RL. Sclerostin: current knowledge and future perspectives. Calcif tissue Int. 2010;87:99–107.
9. Appelman-Dijkstra NM, Papapoulos SE. Sclerostin inhibition in the management of osteoporosis. Calcif Tissue Int. 2016;98:370–80.
10. Lewiecki EM. Sclerostin: a novel target for intervention in the treatment of osteoporosis. Discov Med. 2011;12:263–73.
11. Rachner TD, Khosla S, Hofbauer LC. Osteoporosis: now and the future. Lancet. 2011;377:1276–87.
12. van Bezooijen RL, ten Dijke P, Papapoulos SE, Lowik CW. SOST/sclerostin, an osteocyte-derived negative regulator of bone formation. Cytokine Growth Factor Rev. 2005;16:319–27.
13. Hesse E, Schroder S, Brandt D, Pamperin J, Saito H, Taipaleenmaki H. Sclerostin inhibition alleviates breast cancer-induced bone metastases and muscle weakness. JCI Insight. 2019;5:e125543.
14. Zhu M, Liu C, Li S, Zhang S, Yao Q, Song Q. Sclerostin induced tumor growth, bone metastasis and osteolysis in breast cancer. Sci Rep. 2017;7:11399.
15. Prather C, Adams E, Zentgraf W. Romosozumab: A first-in-class sclerostin inhibitor for osteoporosis. Am J Health Syst Pharm. 2020;77:1949–56.
16. Bandeira L, Lewiecki EM, Bilezikian JP. Romosozumab for the treatment of osteoporosis. Expert Opin Biol Ther. 2017;17:255–63.
17. Cosman F, Crittenden DB, Adachi JD, Binkley N, Czerwinski E, Ferrari S, Hofbauer LC, Lau E, Lewiecki EM, Miyauchi A, et al. Romosozumab treatment in postmenopausal women with osteoporosis. N Engl J Med. 2016;375:1532–43.
18. McClung MR, Brown JP, Diez-Perez A, Resch H, Caminis J, Meisner P, Bolognese MA, Goemaere S, Bone HG, Zanchetta JR, et al. Effects of 24 months of treatment with romosozumab followed by 12 months of denosumab or placebo in postmenopausal women with low bone mineral density: a randomized, double-blind, phase 2, parallel group study. J Bone Miner Res. 2018;33:1397–406.
19. Varghese F, Bukhari AB, Malhotra R, De A. IHC Profiler: an open source plugin for the quantitative evaluation and automated scoring of immunohistochemistry images of human tissue samples. PLoS ONE. 2014;9: e96801.
20. Orthwein T, Huergo LF, Forchhammer K, Selim KA. Kinetic Analysis of a Protein-protein Complex to Determine its Dissociation Constant (KD) and the Effective Concentration (EC50) of an interplaying effector molecule using bio-layer interferometry. Bio Protoc. 2021;11: e4152.
21. Kang Y, Siegel PM, Shu W, Drobnjak M, Kakonen SM, Cordón-Cardo C, Guise TA, Massagué J. A multigenic program mediating breast cancer metastasis to bone. Cancer Cell. 2003;3:537–49.
22. Valdes-Tresanco MS, Valdes-Tresanco ME, Valiente PA, Moreno E. gmx_MMPBSA: a new tool to perform end-state free energy calculations with GROMACS. J Chem Theory Comput. 2021;17:6281–91.
23. Ngan C-H, Hall DR, Zerbe B, Grove LE, Kozakov D, Vajda S. FTSite: high accuracy detection of ligand binding sites on unbound protein structures. Bioinformatics (Oxford, England). 2012;28:286–7.

24. Kozakov D, Grove LE, Hall DR, Bohnuud T, Mottarella SE, Luo L, Xia B, Beglov D, Vajda S. The FTMap family of web servers for determining and characterizing ligand-binding hot spots of proteins. Nat Protoc. 2015;10:733–55.
25. Liu Y, Zhao L, Li W, Zhao D, Song M, Yang Y. FIPSDock: a new molecular docking technique driven by fully informed swarm optimization algorithm. J Comput Chem. 2013;34:67–75.
26. Castro-Mondragon JA, Riudavets-Puig R, Rauluseviciute I, Lemma RB, Turchi L, Blanc-Mathieu R, Lucas J, Boddie P, Khan A, Manosalva Perez N, et al. JASPAR 2022: the 9th release of the open-access database of transcription factor binding profiles. Nucleic Acids Res. 2022;50:D165–73.
27. Naxerova K, Jain RK. Using tumour phylogenetics to identify the roots of metastasis in humans. Nat Rev Clin Oncol. 2015;12:258–72.
28. Minn AJ, Kang Y, Serganova I, Gupta GP, Giri DD, Doubrovin M, Ponomarev V, Gerald WL, Blasberg R, Massague J. Distinct organ-specific metastatic potential of individual breast cancer cells and primary tumors. J Clin Invest. 2005;115:44–55.
29. Sousa S, Clezardin P. Bone-targeted therapies in cancer-induced bone disease. Calcif Tissue Int. 2018;102:227–50.
30. Coleman RE, Croucher PI, Padhani AR, Clezardin P, Chow E, Fallon M, Guise T, Colangeli S, Capanna R, Costa L. Bone metastases. Nat Rev Dis Primers. 2020;6:83.
31. Terpos E, Christoulas D, Katodritou E, Bratengeier C, Gkotzamanidou M, Michalis E, Delimpasi S, Pouli A, Meletis J, Kastritis E, et al. Elevated circulating sclerostin correlates with advanced disease features and abnormal bone remodeling in symptomatic myeloma: reduction post-bortezomib monotherapy. Int J Cancer. 2012;131:1466–71.
32. Kang Y, Siegel PM, Shu W, Drobnjak M, Kakonen SM, Cordon-Cardo C, Guise TA, Massague J. A multigenic program mediating breast cancer metastasis to bone. Cancer Cell. 2003;3:537–49.
33. Arkin MR, Tang Y, Wells JA. Small-molecule inhibitors of protein-protein interactions: progressing toward the reality. Chem Biol. 2014;21:1102–14.
34. Scott DE, Bayly AR, Abell C, Skidmore J. Small molecules, big targets: drug discovery faces the protein-protein interaction challenge. Nat Rev Drug Discov. 2016;15:533–50.
35. Surade S, Blundell TL. Structural biology and drug discovery of difficult targets: the limits of ligandability. Chem Biol. 2012;19:42–50.
36. Jubb H, Higueruelo AP, Winter A, Blundell TL. Structural biology and drug discovery for protein-protein interactions. Trends Pharmacol Sci. 2012;33:241–8.
37. Yu Y, Wang L, Ni S, Li D, Liu J, Chu HY, Zhang N, Sun M, Li N, Ren Q, et al. Targeting loop3 of sclerostin preserves its cardiovascular protective action and promotes bone formation. Nat Commun. 2022;13:4241.